



Effect of TiC addition on SnSb–C composite anodes for sodium-ion batteries



Il Tae Kim ^{a, b}, Sang-Ok Kim ^a, Arumugam Manthiram ^{a, *}

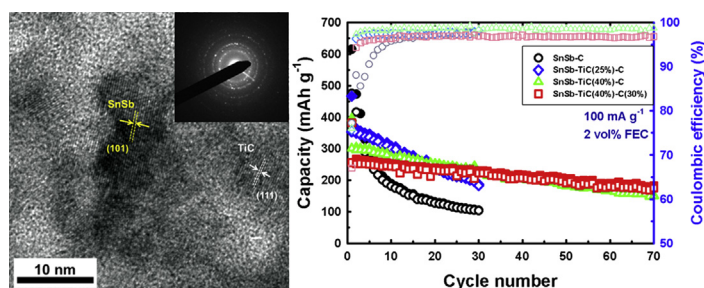
^a Materials Science and Engineering Program and Texas Materials Institute, The University of Texas at Austin, Austin, TX 78712, USA

^b Department of Chemical and Biological Engineering, Gachon University, Seongnam-si, Gyeonggi-do, Republic of Korea

HIGHLIGHTS

- SnSb composites with TiC and C as a matrix were synthesized via HEMM.
- Crystalline phases of SnSb and TiC are identified after HEMM.
- Increase in TiC content leads to better electrochemical performance.
- SnSb–TiC–C demonstrates better cyclability and rate capability compared to SnSb–C.
- The use of FEC additive leads to the longer cyclic- and higher-rate performance.

GRAPHICAL ABSTRACT



ARTICLE INFO

Article history:

Received 5 June 2014

Received in revised form

8 July 2014

Accepted 14 July 2014

Available online 22 July 2014

Keywords:

Sodium-ion batteries

Tin–antimony alloy anodes

Titanium carbide

Electrolyte additives

ABSTRACT

Tin–antimony alloy (SnSb) particles dispersed in a conductive matrix comprised of TiC and carbon have been synthesized by high energy mechanical milling (HEMM) and explored as anodes for sodium-ion batteries. The SnSb–TiC–C samples have been prepared with different TiC and carbon contents in the composite, characterized by X-ray diffraction before and after sodiation and by high-resolution transmission electron microscopy, and compared to SnSb–C as a baseline. The SnSb–TiC–C anodes demonstrate better cyclic performance as well as better rate-capability compared to SnSb–C. In addition, the increase in TiC content in the composite leads to better electrochemical performance. SnSb–TiC(40%)–C(20%) and SnSb–TiC(40%)–C(30%) electrodes exhibit the best electrochemical performance, which could result from both the well-developed SnSb as an electrochemically active nanocrystalline material and the conductive matrix composed of a combination of TiC and carbon. Additionally, the use of FEC electrolyte additive results in much better electrochemical performance even at high-rate current density when combined with this material due to the formation of a stable and thin SEI layer.

© 2014 Elsevier B.V. All rights reserved.

1. Introduction

Wide attention has been recently paid toward sodium-ion batteries (SIBs) as an alternative to lithium-ion batteries (LIBs) due to its low cost, high abundance, and reduction/oxidation potential

only ~0.3 V above that of lithium; particularly, the attention has been towards large-scale energy storage applications [1–5]. Several cathode materials have been examined for SIBs [1,6–9]. In contrast, anodes for SIBs encounter more challenges because of the very low Na-storage capacity of commercial graphite [10]. As a result, hard carbons have been explored as anode materials to realize viable carbon anodes for SIBs [11–13]. In addition, various carbon materials have also been investigated, particularly to increase sodium-ion insertion into carbon-based materials [14,15]. However, the reversibility for carbonaceous materials still remains a major issue

* Corresponding author. Tel.: +1 512 471 1791; fax: +1 512 471 7681.

E-mail addresses: manth@austin.utexas.edu, rmanth@mail.utexas.edu (A. Manthiram).

[11]. Furthermore, the carbon-based anode materials are facing great challenges in association with sodium plating, resulting from their operating voltage close to that of Na/Na^+ . As a result, alternate ways to cope with these challenges arising from utilizing carbonaceous anode materials have been proposed, in which (inter)metallic alloy systems are included [16–21].

Developing (inter)metallic alloy systems as an anode has been extensively considered as a potential strategy for sodium-ion batteries. In these systems, Na ions are capable of reacting with various (inter)metallic elements, such as tin (Sn), antimony (Sb), and germanium (Ge), and forming an alloy during sodiation [16,17]. Sodium-alloys (Na-alloys), however, suffer from enormous volume changes upon uptake or removal of Na (e.g., ~424% for $\text{Na}_{15}\text{Sn}_4$, and ~390% for Na_3Sb), which are even larger than those of the corresponding lithium-alloys (Li-alloys), posing greater limitations for the realization of durable anodes. For example, Ellis et al. [22] developed a sputtered Sn electrode and observed an initial discharge capacity of ~850 mAh g^{-1} . However, this electrode showed rapid cycling-induced capacity degradation to near zero. Yamamoto et al. [23] reported a Sn thin film as an anode for SIBs, which exhibited a charge capacity of 729 mAh g^{-1} in the first cycle; after that, it exhibited a rapid capacity fade after 15 cycles. In addition, Baggetto et al. [24] developed a AlSb thin film electrode prepared via magnetron sputtering for SIBs and LIBs. In the case of SIBs, however, the capacity retention and the kinetics with Na were not satisfactory. In this regard, the exploration of a composite system in which the electrochemically active (inter)metallic components are well-dispersed in a conductive matrix could be an attractive way to realize high-performance sodium-ion batteries.

In the present work, we report the synthesis, electrochemical performance, and sodium-ion storage mechanisms of tin–antimony alloy anodes, SnSb–TiC–C , for sodium-ion cells. The SnSb–C electrode exhibits gradual capacity fading upon cycling. TiC has high electrical conductivity and is denser than carbon, so the combination of TiC with carbon can build a good conductive matrix with high tap density that can lead to lower impedance and better electrochemical performance. Furthermore, the SnSb nanocrystallites dispersed in the TiC–C conductive matrix could overcome the difficulties accompanying alloy anodes since the TiC–C matrix acts as a buffer to absorb the large volume change during the alloying reaction as well as maintains the nanoparticle separation during cycling.

2. Experimental

2.1. Synthesis of SnSb–TiC–C composites

For the preparation of SnSb–TiC–C nanocomposite, precursor powders of Sb:Ti and Sn:Ti with molar ratios of 3:1, 3:2, and 7:13 were prepared by mixing the metallic powders of Sb (99.9%, Alfa Aesar) or Sn (99.9%, Aldrich) and Ti (99.99%, Alfa Aesar) and heat-treating at 600 °C in an Ar atmosphere for 12 h. After that, required amount of Sb–Ti and Sn–Ti powder samples were mixed with stoichiometric amount of acetylene black to form the TiC phase and with 20 wt. % or 30 wt. % excess acetylene black, and subjected to HEMM. For the preparation of SnSb–C , a 1:1 M ratio of Sn and Sb as well as 20 wt. % acetylene black were mixed, followed by HEMM. The SnSb–TiC–C sample with 30 wt. % carbon content in the composite is marked as C(30%). Otherwise, the carbon content in the composites is 20 wt. %. The powder mixtures were placed in hardened steel vials (80 cm^3 capacity) with steel balls of diameter 1/2 and 1/4 in. at a ball : powder mass ratio of 20:1. All HEMM process was carried out at a speed of 500 rpm under Argon atmosphere with a Fritsch Pulverisette 6 planetary mill. The milling times for SnSb–C and SnSb–TiC–C were both 40 h. The TiC content

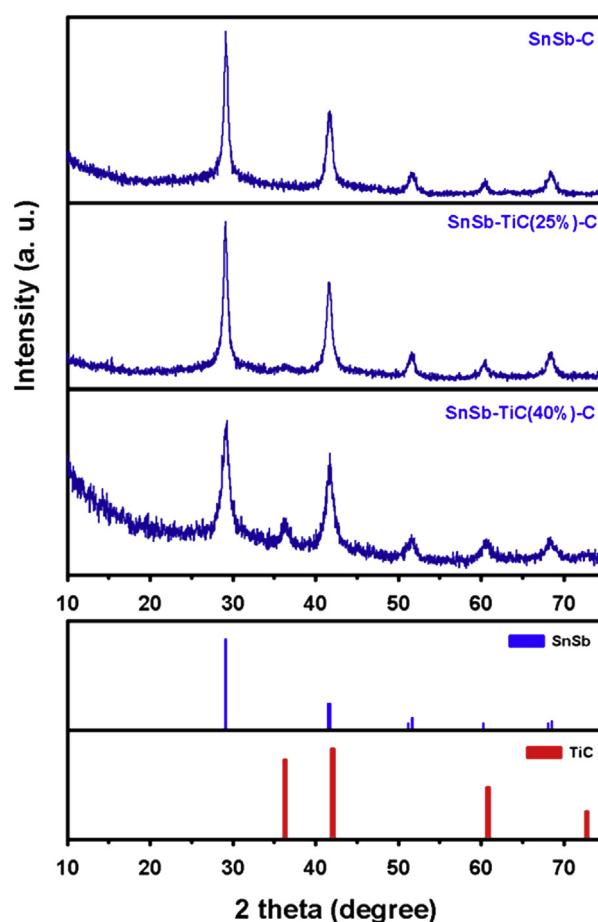


Fig. 1. XRD patterns of SnSb–C , SnSb–TiC(25%)–C , and SnSb–TiC(40%)–C composites, with the reference peaks of SnSb and TiC indicated.

was controlled by changing the molar ratio of Sn:Ti and Sb:Ti and introducing required amount of stoichiometric carbon to give 25, 40, and 65 wt. % TiC in the composite.

2.2. Materials characterization

The as-prepared samples were examined with a Rigaku RINT 2000 diffractometer and Cu $K\alpha$ radiation in the range of 10–70° with a scan rate of $0.03^\circ \text{ s}^{-1}$ for structural characterization. The *ex situ* XRD measurements were conducted with the tested electrochemical cells at different states of charge. The electrodes were disassembled in an Ar-filled glove box and rinsed with anhydrous dimethyl carbonate to remove the residual salts. The nanostructure and composition of the powder samples were characterized with a JEOL 2010F transmission electron microscope.

2.3. Electrochemical measurements

For the measurements of electrochemical performance, electrodes were prepared on Cu foils with slurries comprised of 70 wt. % active material, 15 wt. % Super P, 15 wt. % PVDF, and *N*-methylpyrrolidone (NMP). The electrodes were dried at 60 °C for 3 h in an oven and at 120 °C overnight in a vacuum oven. The cells were assembled with sodium as the counter electrode, a sample electrode as the working electrode, 1 M NaClO_4 in a mixture of ethylene carbonate (EC)/propylene carbonate (PC) (1:1 by volume) as the electrolyte, and a glass separator (APFA from Millipore). For a comparison, 2 vol. % of fluoroethylene carbonate (FEC) was

introduced as an electrolyte additive. The test electrodes had an active material (SnSb) content of 1–1.5 mg, but the capacity values were calculated based on the total weight of the composite (SnSb + TiC + C). The galvanostatic charge/discharge experiments were carried out at a constant current density of 100 mA g^{-1} at 0.0–1.5 V vs. Na/Na⁺. Electrochemical impedance spectroscopy (EIS) analysis was conducted with a Solartron SI 1260 instrument with an applied amplitude of 10 mV in the range of 100 kHz to 0.1 Hz after various cycles at 1.5 V vs. Na/Na⁺.

3. Results and discussion

Fig. 1 shows the XRD pattern of the as-prepared SnSb–C and SnSb–TiC–C composites. In the case of the SnSb–C composite, the pattern shows pure SnSb crystalline phase, with no pure Sb and Sn peaks, and amorphous carbon [16]. In the case of SnSb–TiC–C,

additional TiC peaks at around 36.3° (111) and 60.8° (220) are observed [25]. The peak intensity increases with increasing TiC wt. % (from 25% to 40%) as seen in Fig. 1. The SnSb–TiC–C composites also display only pure SnSb and TiC phases with no Sn, Sb, and Ti phases, illustrating that the reactions to form SnSb and TiC nanocrystallites are completed during HEMM.

The morphology results are given in Fig. 2. The SnSb and TiC nanoparticles are well dispersed in the carbon matrix (Fig. 2a). The high resolution transmission electron microscopy (HRTEM) images illustrate interplanar spacings of 0.31 and 0.25 nm, respectively, corresponding to the (101) planes of SnSb and (111) planes of TiC.

Fig. 3 compares the initial discharge and charge voltage profiles of SnSb–C and SnSb–TiC–C electrodes at a current rate of 100 mA g^{-1} . The SnSb–C electrode exhibits the highest charge capacity of 475 mAh g^{-1} . When increasing the TiC content in the composite, which is an electrochemically inactive component (see Fig. S1 in Supporting information), the charge capacity decreases due to the decrease in the weight percent of the electrochemically active component (SnSb) in the composite; for instance, SnSb–TiC(25%)–C has an initial charge capacity of 388 mAh g^{-1} while SnSb–TiC(40%)–C has 325 mAh g^{-1} . Nevertheless, the addition of the TiC into SnSb–C leads to better electrochemical performance due to its high conductivity, resulting in small increase in impedance, and well-dispersed characteristics as a matrix component (discussed later). In addition, when increasing the carbon content while maintaining the same TiC content in the composite, the initial charge capacity decreases as well. For example, SnSb–TiC(40%)–C(20%) delivers a higher initial charge capacity (325 mAh g^{-1}) than SnSb–TiC(40%)–C(30%) (305 mAh g^{-1}). Specifically, the capacity values of carbon in sodium-ion cells differ depending on the experimental conditions including synthesis process, voltage range, electrolyte used, type of carbon, etc. Ponrouch et al. [13] reported that the capacity range of the as-prepared carbon varies $\sim 200 \text{ mAh g}^{-1}$ to $\sim 300 \text{ mAh g}^{-1}$ based on the specific surface area and degree of graphitization. We found the initial charge capacity of the acetylene black after milling for 40 h to be $\sim 220 \text{ mAh g}^{-1}$ (see Fig. S2 in Supporting information). However, the capacity contribution of carbon could vary in the range of $200\text{--}300 \text{ mAh g}^{-1}$ when the carbon matrix is developed with active materials (e.g., SnSb) and other matrices (e.g., TiC). The initial capacities of the SnSb–TiC(40%)–C(30%) electrodes with three different cells were found to be in the range of 300 mAh g^{-1} to 307 mAh g^{-1} . Taking the initial charge capacity of SnSb–TiC(40%)–C(30%) as 303 mAh g^{-1} and assuming an initial capacity contribution of $\sim 260 \text{ mAh g}^{-1}$ by carbon, the calculated capacity value of SnSb is $\sim 750 \text{ mAh g}^{-1}$ ($(750 \times 0.3) + (260 \times 0.3) = 303 \text{ mAh g}^{-1}$).

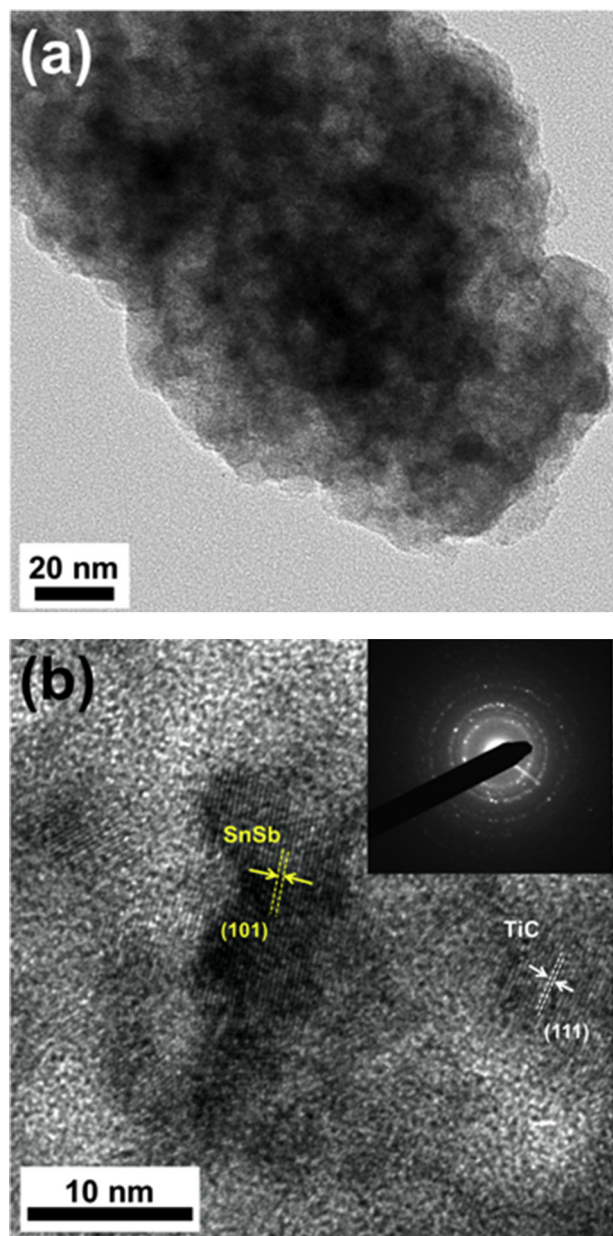


Fig. 2. (a) TEM image of SnSb–TiC–C nanocomposite. (b) High-resolution TEM image of SnSb–TiC–C nanocomposite, with the inset showing the electron diffraction pattern over the selected region.

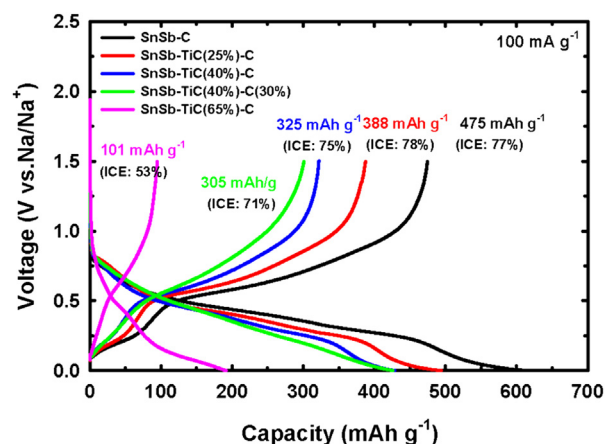


Fig. 3. Initial voltage profiles of SnSb–C and SnSb–TiC–C electrodes with different TiC and carbon contents at 100 mA g^{-1} .

The sodiation/desodiation reactions can be evaluated from the differential capacity plots as shown in Fig. 4. During the first discharge (sodiation) scan, broad irreversible peaks around 0.8 and 0.5 V are observed. They are ascribed to the irreversible decomposition of the electrolyte and formation of solid-electrolyte interphase (SEI) layer on the surface of the composite. During the second discharge scan, four peaks are observed at 0.57, 0.37, 0.27, and 0.00 V. In the reverse charge (desodiation) scan, four peaks

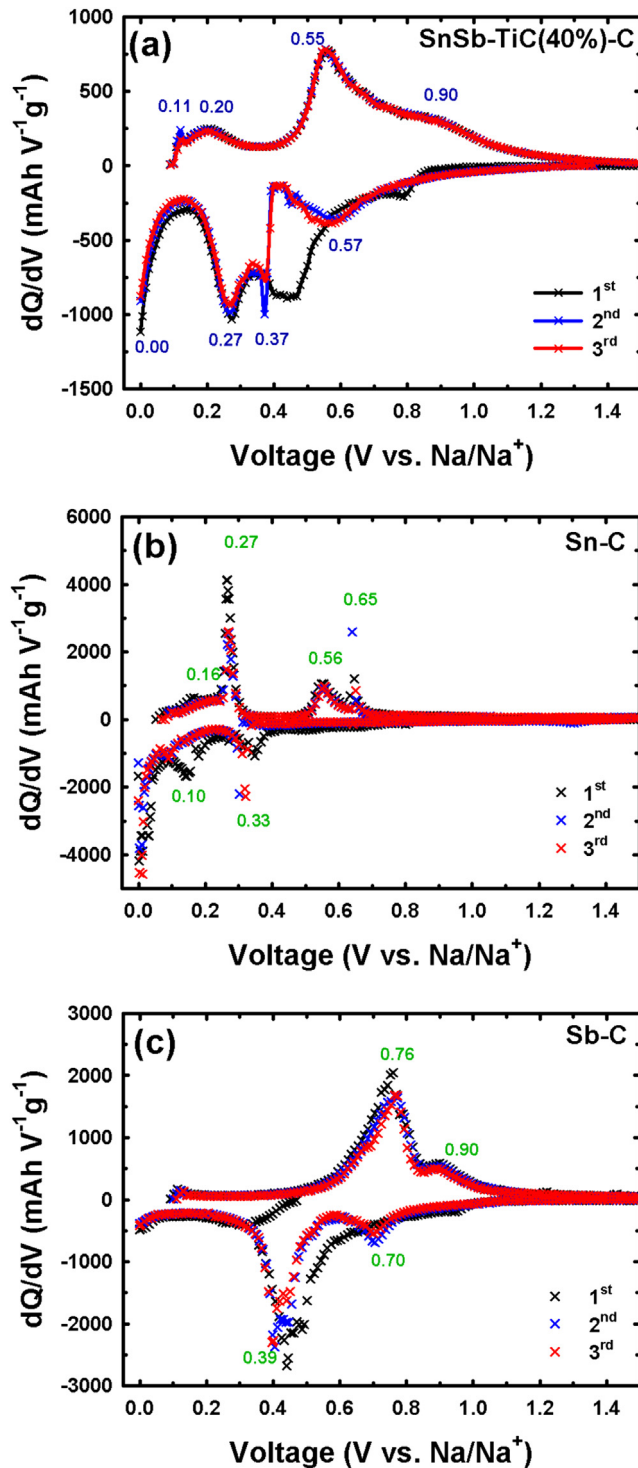


Fig. 4. Differential capacity plots of (a) SnSb–TiC(40%)–C, (b) Sn–C, and (c) Sb–C electrodes between 0.0 V and 1.5 V.

centered at 0.11, 0.20, 0.55, and 0.90 V are detected as well. It is noted that the electrochemical mechanism of SnSb with Na is not the simple addition of those of Sn and Sb with Na [26]. The reaction of SnSb with Na occurs at different potentials compared to those observed for Sn–C and Sb–C as shown in Fig. 4b and c. Based on the differential capacity plots of Sn–C and Sb–C electrodes, the two peaks at ~ 0.00 and 0.27 V can be assigned to the sodium-ion reaction with acetylene black carbon and sodium–tin (Na–Sn). The peaks at 0.37 V mainly corresponds to the sodium–antimony (Na–Sb) alloying reaction along with the Na–Sn alloying reaction. Furthermore, the broad peak centered at 0.57 V is related to the Na–Sb alloying reaction. In the charge scan, the peaks at 0.11 and 0.20 V are ascribed to the sodium-ion extraction out of acetylene black carbon and Na–Sn. In addition, the peak centered at 0.55 V with a broad shoulder up to 0.76 V can be ascribed to the overlapping of the Na–Sn and Na–Sb dealloying reactions, while the peak at 0.90 V is due to the Na–Sb dealloying reaction. This sodiation/desodiation mechanism of SnSb–TiC–C electrodes was further examined by *ex situ* XRD as illustrated in Fig. 5. When discharged to 0 V vs. Na/Na⁺ (full sodiation), additional peaks can be observed at around 31.9° and 38.6°, which correspond to the formation of, respectively, Na₁₅Sn₄ and Na₃Sb alloys, while the SnSb peaks disappear. In addition, there are still remaining peaks at 36.2° and 42.0° at 0 V, which are related to the TiC crystalline peaks, illustrating that TiC is persistent throughout the sodiation. When fully desodiated (1.5 V vs. Na/Na⁺), the phases of Na₁₅Sn₄ and Na₃Sb disappear, while crystalline SnSb peaks appear again along with the unchanged TiC peaks, illustrating that crystalline SnSb phase is reversible during cycling.

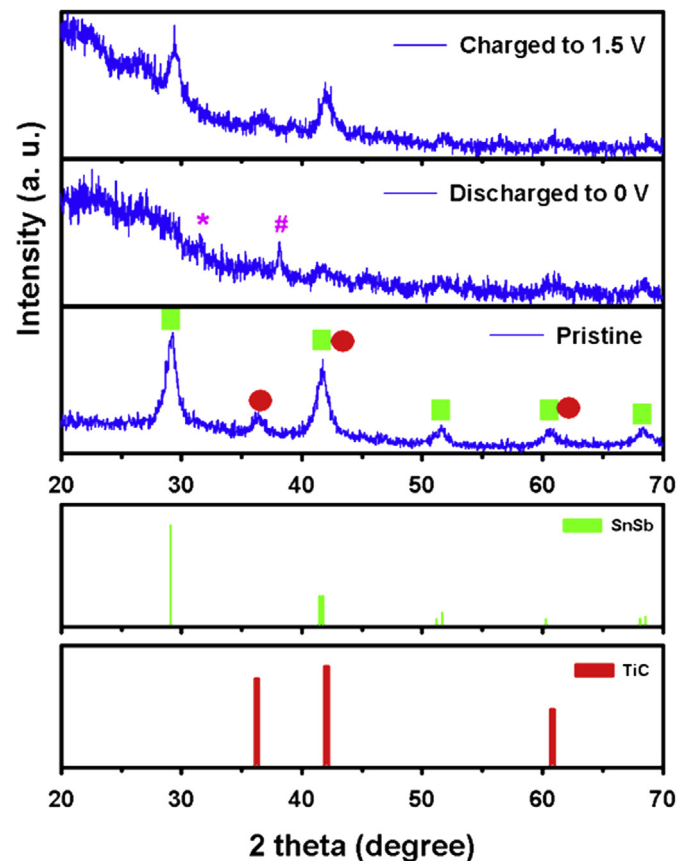


Fig. 5. *Ex-situ* XRD patterns of SnSb–TiC–C composite anodes before cycling, after full sodiation (0 V), and after full desodiation (1.5 V). The * represents the formation of Na₁₅Sn₄ phase and the # corresponds to the formation of Na₃Sb phase.

Fig. 6 shows the cyclability of SnSb–C and SnSb–TiC–C electrodes at a current rate of 100 mA g^{-1} . The solid symbols represent the discharge capacity of the as-prepared electrode materials while the open symbols correspond to their charge capacity. The electrodes with FEC additive exhibit lower capacities than those without FEC additive. The addition of FEC leads to a decomposition at $\sim 0.8 \text{ V}$ in the first discharge and leads to the formation of a stable SEI layer, which results in a slightly lower initial discharge capacity [27]. In addition, there is no significant difference in the initial Coulombic efficiency before and after FEC addition. Therefore, the electrode with FEC additive exhibits lower charge capacity than that without FEC additive (see Fig. S3 in Supporting information). In the case of SnSb–C electrode, gradual capacity fade occurs during cycling. By increasing the TiC content in the composite, the cyclability of SnSb–TiC–C electrodes becomes better than that of the SnSb–C electrode. In the case of SnSb–TiC(65%)–C composite anode, stable cyclability is seen; however, due to the large amount of TiC in the composite, it only exhibits a charge capacity of 100 mAh g^{-1} . The SnSb–TiC(25%)–C composite anode delivers a charge capacity of 150 mAh g^{-1} at 30 cycles, which corresponds to a capacity retention of 40%, while the SnSb–C exhibits a capacity retention of only 22% at 30 cycles. When the TiC content in the composite is increased to 40 wt. %, the SnSb–TiC(40%)–C electrode shows a charge capacity of 210 mAh g^{-1} at 30 cycles corresponding to a capacity retention of 65%. Furthermore, when the carbon content increases from 20% to 30% with the same TiC content of 40%, the SnSb–TiC(40%)–C(30%) electrode delivers a capacity of 215 mAh g^{-1} , which represents a capacity retention of 71% at 30 cycles. This superior performance could be attributed

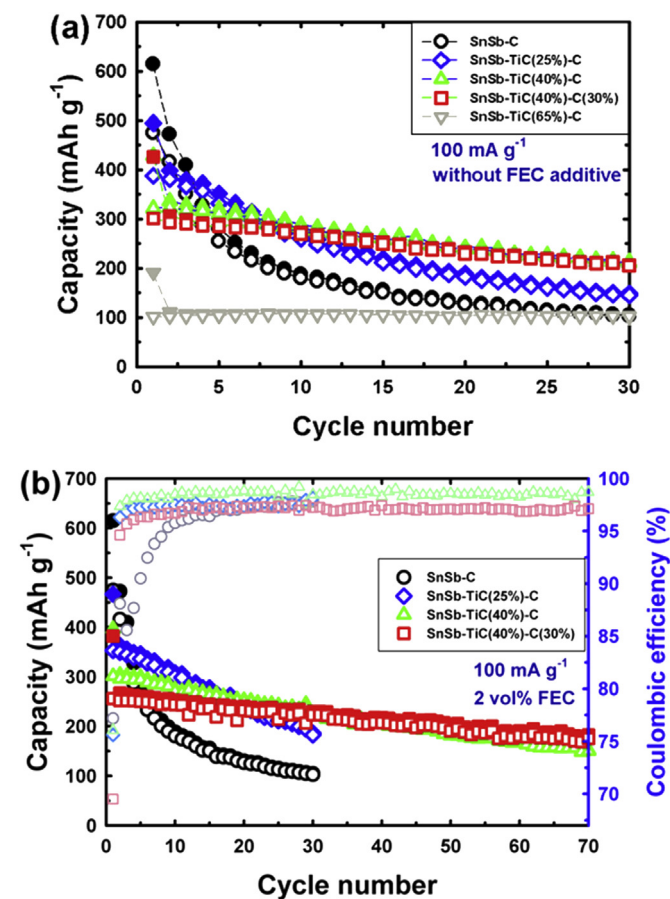


Fig. 6. Comparison of the cyclic performances of SnSb–C and SnSb–TiC–C with different TiC and carbon contents (a) without and (b) with 2 vol. % of FEC additive at 100 mA g^{-1} .

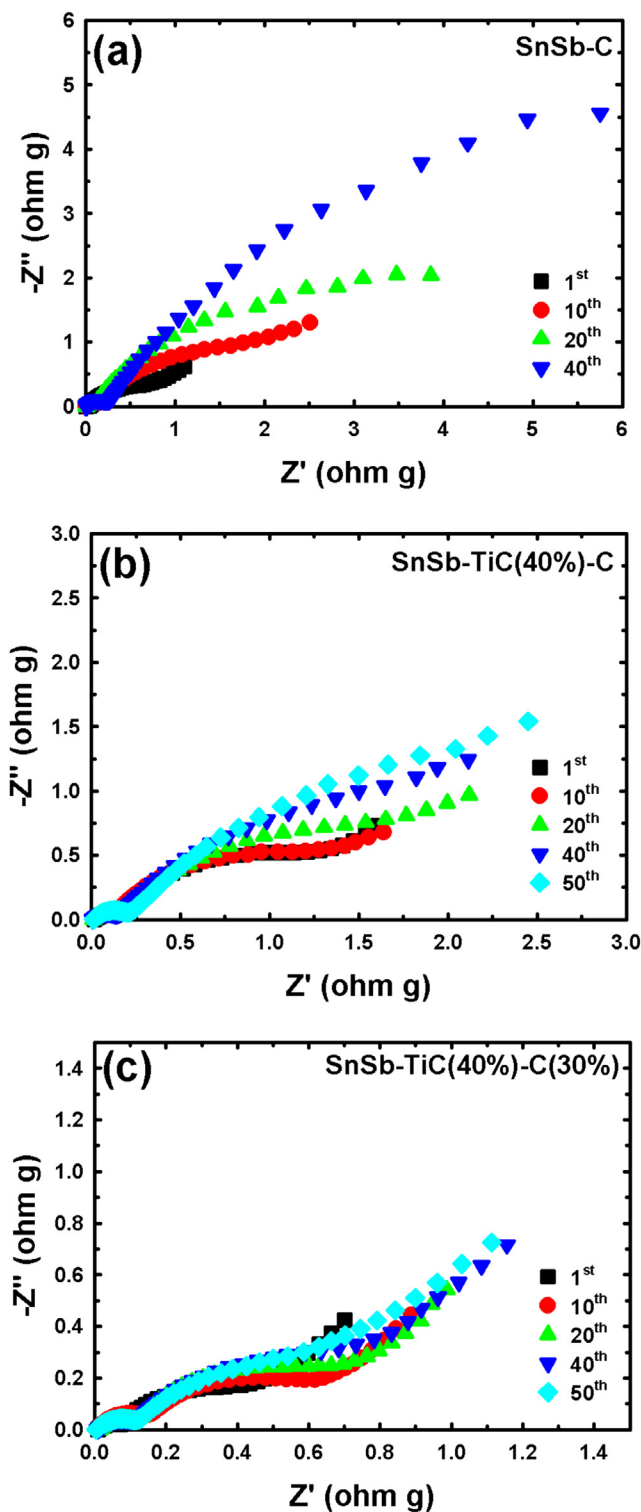


Fig. 7. Electrochemical impedance spectra (EIS) of (a) SnSb–C, (b) SnSb–TiC(40%)–C, and (c) SnSb–TiC(40%)–C(30%) electrodes.

to the incorporation of a hybrid conductive matrix consisting of TiC and carbon, resulting in low impedance. In addition, it is noted that when 2 vol. % of FEC additive is introduced into the electrolyte, the SnSb–TiC–C electrodes exhibit longer cyclic life as illustrated in Fig. 6b. In contrast, the SnSb–C anode does not exhibit stable cyclability even when adding the FEC additive into the electrolyte. The SnSb–TiC(25%)–C electrode cycled with FEC shows better cyclability

Table 1

Comparison of the SEI film resistance (R_s) and charge transfer resistance (R_{ct}) of SnSb–C, SnSb–TiC(40%)–C, and SnSb–TiC(40%)–C(30%) electrodes at 1st and 40th cycle.

	R_s^{1st} (ohm g)	R_s^{40th} (ohm g)	Increase (%)	R_{ct}^{1st} (ohm g)	R_{ct}^{40th} (ohm g)	Increase (%)
SnSb–C	0.056	0.296	429	0.984	14.58	1382
SnSb–TiC(40%)–C	0.081	0.173	114	1.203	3.152	162
SnSb–TiC(40%)–C(30%)	0.085	0.144	69	0.531	1.083	104

than the SnSb–TiC(25%)–C electrode without FEC additive, but it still shows gradual decay in capacity. On the other hand, when cycled with FEC additive, the SnSb–TiC(40%)–C electrode shows a capacity retention of 55% at 70 cycles, while the SnSb–TiC(40%)–C(30%) electrode demonstrates a capacity retention of 73% at 70 cycles. This result could be due to a thin and stable SEI layer formation on the electrode surface during prolonged cycling [27,28].

The cyclic performance was further investigated with electrochemical impedance spectroscopic plots. Each plot consists of two semicircles and one slope. The first semicircle in the high-frequency region is related to the interfacial layer of the electrodes, while the second semicircle in the medium-frequency region corresponds to the charge-transfer reaction between the active-anode mass and sodium at the electrode surface. The slope in the low-frequency region is attributed to the sodium-ion diffusion through the bulk material. The intercept of the first semicircle with the real axis is related to the ohmic resistance, and the

diameter of the second semicircle represents the charge-transfer resistance. When observing the EIS spectra at various cycle numbers, the SnSb–C electrode exhibits great increase in impedance even at low cycle numbers as seen in Fig. 7a, illustrating a significant increase in SEI film resistance (R_s) and charge transfer resistance (R_{ct}) during cycling. In contrast, the SnSb–TiC(40%)–C electrodes show smaller increase in impedance as illustrated in Fig. 7b and c than the SnSb–C electrode. The EIS data are summarized in Table 1. In the case of SnSb–C electrode, the % increases in R_s and R_{ct} between the initial and the 40th cycle are, respectively, 429% and 1382%, revealing a significant increase in impedance. On the other hand, the SnSb–TiC(40%)–C and SnSb–TiC(40%)–C(30%) electrodes exhibit much smaller increase in impedance between the initial and the 40th cycle as shown in Table 1. Therefore, the electrodes with TiC as a matrix exhibit lower impedance as discussed, and it is confirmed that SnSb–TiC–C electrodes show better electrochemical performance than SnSb–C.

When looking at the rate capability of the as-prepared electrodes as shown in Fig. 8, the SnSb–TiC–C electrodes display better rate capability than SnSb–C. The electrodes demonstrating better cyclic performance exhibit better rate performance. The SnSb–C electrode shows poor rate capability similar to the inferior cycling performance seen in Fig. 6. On the other hand, the electrodes with TiC exhibit better rate capability. The SnSb–TiC(25%)–C electrode delivers a capacity of 200 mAh g^{−1} at a current rate of 3000 mA g^{−1}, demonstrating a capacity retention of 50% when normalized by the capacity at 100 mA g^{−1}. The SnSb–TiC(40%)–C electrodes demonstrate much better rate capabilities of 220 mAh g^{−1} for SnSb–TiC(40%)–C and 230 mAh g^{−1}

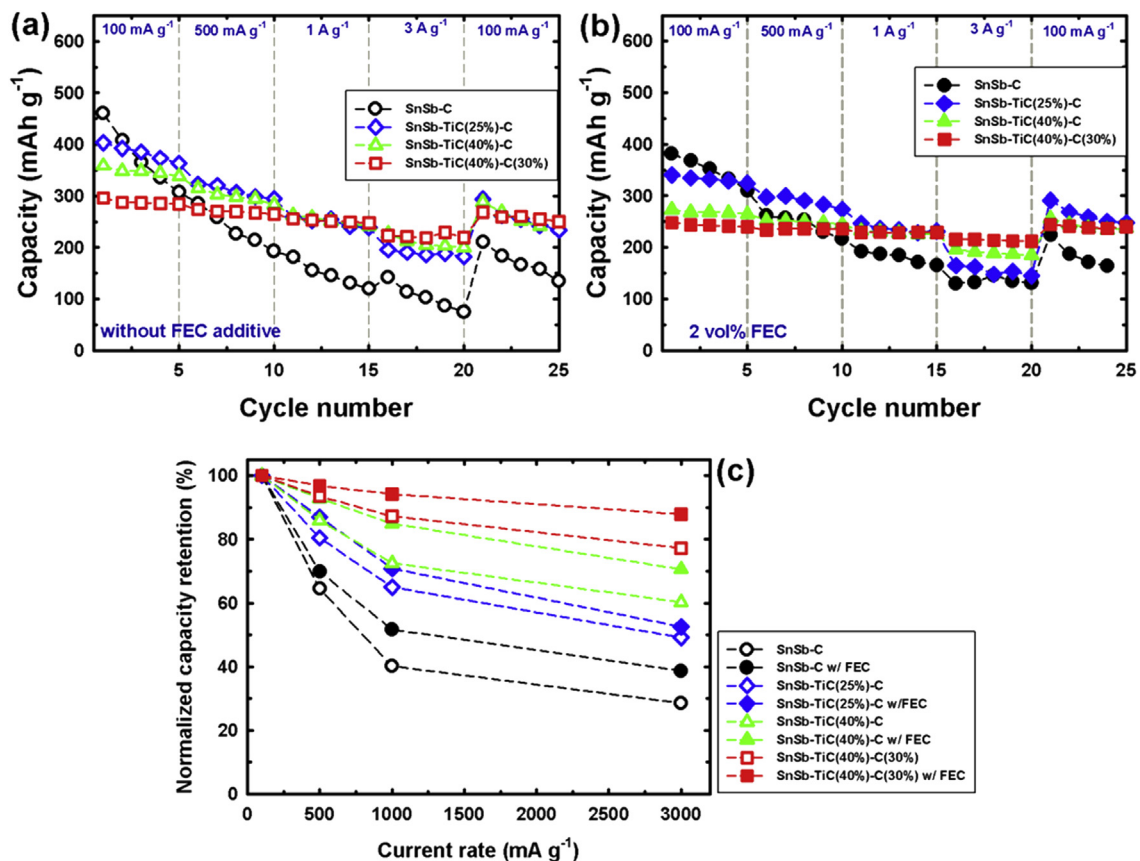


Fig. 8. Rate cyclic performance of SnSb–C and SnSb–TiC–C with different TiC and carbon contents (a) without and (b) with 2 vol. % of FEC additive at various current rates. (c) Normalized % charge capacity retention values of SnSb–C and SnSb–TiC–C with different TiC and carbon contents before and after introducing 2 vol. % of FEC additive into the electrolyte.

for SnSb–TiC(40%)–C(30%) at 3000 mA g^{−1}, which correspond to a capacity retention of, respectively, 61% and 78%, as illustrated in Fig. 8c. Furthermore, when introducing 2 vol. % of FEC additive into the electrolyte, the as-prepared electrodes exhibit higher-rate capability as shown in Fig. 8b and c. The capacity retentions of SnSb–TiC(25%)–C, SnSb–TiC(40%)–C, and SnSb–TiC(40%)–C(30%) at 3000 mA g^{−1} are 54%, 72%, and 88%, respectively, when cycled with FEC additive. This high-rate capability could be due to the formation of more stable and thin SEI layer when adding 2 vol. % of FEC additive together with the smaller charge-transfer resistance, better dispersion of the particles upon cycling [28,29].

4. Conclusions

SnSb–TiC–C nanocomposites with different TiC contents synthesized via HEMM have been examined as anode materials for sodium-ion cells. The introduction of TiC into the composite leads to better cyclability as well as high-rate performance compared to the SnSb–C composite without TiC. Specifically, the SnSb–TiC(40%)–C electrode exhibits good cyclability with 210 mAh g^{−1} at 100 mA g^{−1} after 30 cycles and a normalized capacity retention of ~61% on increasing the current rate to 3000 mA g^{−1}. Furthermore, when increasing the carbon content to 30% with the same TiC content of 40%, the SnSb–TiC(40%)–C(30%) electrode demonstrates better cyclic performance and higher rate capability with a capacity retention of 78% at 3000 mA g^{−1}. When 2 vol. % FEC additive is introduced into the electrolyte, the SnSb–TiC(40%)–C (30%) electrode exhibits longer cyclic life with a capacity retention of 73% at 70 cycles and superior rate capability with ~88% retention at 3000 mA g^{−1}. This enhanced electrochemical performance could be mainly pertinent to thin and stable SEI layer formation along with smaller charge-transfer resistance and better dispersion of the electrochemically active material in the conductive matrix of TiC and carbon. Nevertheless, the electrodes with TiC addition still suffer from capacity decay, which might result from the large volume change that the TiC–C matrix cannot endure. Our future work will focus on developing better matrix combinations for accommodating the volume changes more efficiently with sodium-ion cells.

Acknowledgments

This work was supported by the U.S. Department of Energy, Office of Basic Energy Sciences, Division of Materials Sciences and Engineering under award number DE-SC0005397.

Appendix A. Supplementary data

Supplementary data related to this article can be found at <http://dx.doi.org/10.1016/j.jpowsour.2014.07.081>.

References

- [1] B.L. Ellis, L.F. Nazar, *Curr. Opin. Solid State Mater.* 16 (2012) 168–177.
- [2] N. Yabuuchi, M. Kajiyama, J. Iwatate, H. Nishikawa, S. Hitomi, R. Okuyama, R. Usui, Y. Yamada, S. Komaba, *Nat. Mater.* 11 (2012) 512–517.
- [3] X.C. Lu, G.G. Xia, J.P. Lemmon, Z.G. Yang, *J. Power Sources* 195 (2010) 2431–2442.
- [4] S.P. Ong, V.L. Chevrier, G. Hautier, A. Jain, C. Moore, S. Kim, X. Ma, G. Ceder, *Energy Environ. Sci.* 4 (2011) 3680–3688.
- [5] S. Komaba, W. Murata, T. Ishikawa, N. Yabuuchi, T. Ozeki, T. Nakayama, A. Ogata, K. Gotoh, K. Fujiwara, *Adv. Funct. Mater.* 21 (2011) 3859–3867.
- [6] K.-H. Ha, S.H. Woo, D. Mok, N.-S. Choi, Y. Park, S.M. Oh, Y. Kim, J. Kim, J. Lee, L.F. Nazar, K.T. Lee, *Adv. Energy Mater.* 3 (2013) 770–776.
- [7] R. Berthelot, D. Carlier, C. Delmas, *Nat. Mater.* 10 (2011) 74–80.
- [8] Y. Lu, L. Wang, J. Cheng, J.B. Goodenough, *Chem. Commun.* 48 (2012) 6544–6546.
- [9] R. Tripathi, G.R. Gardiner, M.S. Islam, L.F. Nazar, *Chem. Mater.* 23 (2011) 2278–2284.
- [10] A.G. Metrot, D. Billaud, A. Herold, *Synth. Met.* 1 (1980) 363–369.
- [11] R. Alcantara, J.M. Jimenez-Mateos, P. Lavela, J.L. Tirado, *Electrochem. Commun.* 3 (2001) 639–642.
- [12] X. Xia, M.N. Obrovac, J.R. Dahn, *Electrochem. Solid-State Lett.* 14 (2011) A130–A133.
- [13] A. Ponrouch, A.R. Goni, M. Rosa Palacin, *Electrochem. Commun.* 27 (2013) 85–88.
- [14] Y. Cao, L. Xiao, M.L. Sushko, W. Wang, B. Schwenzer, J. Xiao, Z. Nie, L.V. Saraf, Z. Yang, J. Liu, *Nano Lett.* 12 (2012) 3783–3787.
- [15] D.A. Stevens, J.R. Dahn, *J. Electrochem. Soc.* 147 (2000) 1271–1273.
- [16] L. Xiao, Y. Cao, J. Xiao, W. Wang, L. Kovarik, Z. Nie, J. Liu, *Chem. Commun.* 48 (2012) 3321–3323.
- [17] L. Baggetto, J.K. Keum, J.F. Browning, G.M. Veith, *Electrochem. Commun.* 34 (2013) 41–44.
- [18] X. Zhou, Z. Dai, J. Bao, Y.-G. Guo, *J. Mater. Chem. A* 1 (2013) 13727–13731.
- [19] L. Baggetto, P. Ganesh, C.-N. Sun, R.A. Meisner, T.A. Zawodzinski, G.M. Veith, *J. Mater. Chem. A* 1 (2013) 7985–7994.
- [20] L. Wu, P. Pei, R. Mao, F. Wu, Y. Wu, J. Qian, Y. Cao, X. Ai, H. Yang, *Electrochim. Acta* 87 (2013) 41–45.
- [21] L. Wu, X. Hu, J. Qian, F. Pei, F. Wu, R. Mao, X. Ai, H. Yang, Y. Cao, *Energy Environ. Sci.* 7 (2014) 323–328.
- [22] L.D. Ellis, P.P. Ferguson, M.N. Obrovac, *J. Electrochem. Soc.* 160 (2013) A869–A872.
- [23] T. Yamamoto, T. Nohira, R. Hagiwara, A. Fukunaga, S. Sakai, K. Nitta, S. Inazawa, *J. Power Sources* 217 (2012) 479–484.
- [24] L. Baggetto, M. Marszewski, J. Gorka, M. Jaroniec, G.M. Veith, *J. Power Sources* 243 (2013) 699–705.
- [25] X.Z. Zhu, Kunyu, Baochang Cheng, Qiushi Lin, Xiuqin Zhang, Tieli Chen, Yunsheng Su, *Mater. Sci. Eng. C* 16 (2001) 103–105.
- [26] A. Darwiche, M.T. Sougrati, B. Fraisse, L. Stievano, L. Monconduit, *Electrochem. Commun.* 32 (2013) 18–21.
- [27] S. Komaba, T. Ishikawa, N. Yabuuchi, W. Murata, A. Ito, Y. Ohsawa, *ACS Appl. Mater. Interfaces* 3 (2011) 4165–4168.
- [28] L. Liao, X. Cheng, Y. Ma, P. Zuo, W. Fang, G. Yin, Y. Gao, *Electrochim. Acta* 87 (2013) 466–472.
- [29] S. Park, J.H. Ryu, S.M. Oh, *J. Electrochem. Soc.* 158 (2011) A498–A503.